LETTERS
https://doi.org/10.1038/s41563-020-0665-0

nature materials

Broad spectral tuning of ultra-low-loss polaritons in a van der Waals crystal by intercalation

Javier Taboada-Gutiérrez[1,2], Gonzalo Álvarez-Pérez[1,2], Jiahua Duan[1,2], Weiliang Ma[3], Kyle Crowley[4], Iván Prieto[5], Andrei Bylinkin[6,7], Marta Autore[7], Halyna Volkova[8], Kenta Kimura[9], Tsuyoshi Kimura[9], M.-H. Berger[8], Shaojuan Li[10], Qiaoliang Bao[3,10], Xuan P. A. Gao[4], Ion Errea[6,11,12], Alexey Y. Nikitin[6,13], Rainer Hillenbrand[7,13], Javier Martín-Sánchez[1,2] ✉ and Pablo Alonso-González[1,2] ✉

Phonon polaritons—light coupled to lattice vibrations—in polar van der Waals crystals are promising candidates for controlling the flow of energy on the nanoscale due to their strong field confinement, anisotropic propagation and ultra-long lifetime in the picosecond range[1–5]. However, the lack of tunability of their narrow and material-specific spectral range—the Reststrahlen band—severely limits their technological implementation. Here, we demonstrate that intercalation of Na atoms in the van der Waals semiconductor α-V_2O_5 enables a broad spectral shift of Reststrahlen bands, and that the phonon polaritons excited show ultra-low losses (lifetime of 4 ± 1 ps), similar to phonon polaritons in a non-intercalated crystal (lifetime of 6 ± 1 ps). We expect our intercalation method to be applicable to other van der Waals crystals, opening the door for the use of phonon polaritons in broad spectral bands in the mid-infrared domain.

In recent years, polar van der Waals (vdW) crystals have become excellent platforms to study and manipulate light on the nanoscale[6–9], the goal of the burgeoning field of nano-optics. Their reduced dimensionality and intrinsic anisotropy have allowed the discovery of infrared-active phonon polaritons (PhPs)—light coupled to lattice vibrations—with extraordinary properties. Prominent examples are PhPs in the dielectric hexagonal boron nitride (h-BN)—which uncover ultra-strong confinement, slow propagation and out-of-plane hyperbolic behaviour, allowing the observation of exotic optical phenomena such as ray propagation or hyper-lensing effects[10]—and in the polar vdW semiconductor α-MoO_3—revealing in-plane anisotropic propagation (hyperbolic or elliptic) with ultra-low losses[2] (lifetimes of 8 ps)—offering opportunities for planar nanotechnologies aiming a directional control of light–matter interactions at the nanoscale.

However, despite the extraordinary properties of these PhPs in vdW crystals, there is still an important technological drawback for their implementation into nanophotonics technologies, namely the narrow and material-dependent spectral band where they exist (the so-called Reststrahlen band (RB), defined between the transverse and longitudinal optic phonon frequencies). Although attempts to spectrally tune the RB in bulk polar materials have been recently tackled[11,12], a broad spectral tuning of a RB in a polar vdW material, and consequently of the PhPs supported within it, has remained elusive.

In this work, we introduce intercalation as an efficient route to spectrally tune PhPs in a polaritonic vdW crystal, the metal oxide α-V_2O_5. By near-field imaging of Na-intercalated α-V_2O_5 (forming the crystal α'-(Na)V_2O_5) we reveal a RB shift of ~30 cm^{-1} (60% of the initial RB width), and consequently of the PhPs supported within it. PhPs in the intercalated α'-(Na)V_2O_5 crystal exhibit ultra-low loss (lifetimes of 4 ± 1 ps) and in-plane anisotropic propagation, similar to PhPs in pristine α-V_2O_5 (lifetimes of 6 ± 1 ps), evidencing that the intercalation of atoms in between the vdW layers does not substantially affect the polaritonic properties of the crystal.

The optical image in Fig. 1a shows the characteristic rectangular shape of α-V_2O_5 thin flakes studied in this work. This asymmetric geometry is inherited from the strong anisotropy of its crystal lattice[13,14], which is illustrated in the diagram of Fig. 1b. As can be seen, the crystalline unit cell of α-V_2O_5 shows an orthorhombic structure where the three inequivalent oxygen positions (denoted O_{1-3}) with respect to the vanadium atom give rise to asymmetric V–O bonds along the three different crystalline axes. This strong biaxial anisotropy is also translated into the optical properties of the crystal (Supplementary Information) as observed in Fig. 1c, where the dielectric permittivity of α-V_2O_5 (ref. [15]) along the three crystalline axes is shown. We can see up to three spectral bands in the plotted range (in colour) where at least one of the permittivity components is negative, thus indicating the existence of three RBs (denoted RB_{1-3}) and the possibility of supporting PhPs within them. Given that only one (as in RB_1 and RB_3) or two (as in RB_2) components of the permittivity are negative, instead of the three components (as in isotropic media), PhPs in α-V_2O_5 are expected to be strongly anisotropic with either elliptical or hyperbolic propagation[2,5,16,17].

To probe the excitation of PhPs in α-V_2O_5, we performed polariton interferometry[18,19] using scattering-type scanning near-field

[1]Departamento de Física, Universidad de Oviedo, Oviedo, Spain. [2]Nanomaterials and Nanotechnology Research Center (CINN-CSIC), El Entrego, Spain. [3]State Key Laboratory of Functional Materials for Informatics, Shanghai Institute of Microsystem and Information Technology, Chinese Academy of Sciences, Shanghai, China. [4]Department of Physics, Case Western Reserve University, Cleveland, OH, USA. [5]Institute of Science and Technology Austria, Klosterneuburg, Austria. [6]Donostia International Physics Center (DIPC), Donostia/San Sebastián, Spain. [7]CIC nanoGUNE BRTA and Department of Electricity and Electronics, UPV/EHU, Donostia/San Sebastián, Spain. [8]Centre des Matériaux, CNRS UMR 7633—PSL University, MINES ParisTech, Evry Cedex, France. [9]Department of Advanced Materials Science, University of Tokyo, Kashiwa, Japan. [10]State Key Laboratory of Applied Optics, Changchun Institute of Optics Fine Mechanics and Physics, Chinese Academy of Sciences, Changchun, Jilin, China. [11]Fisika Aplikatua 1 Saila, University of the Basque Country (UPV/EHU), Donostia/San Sebastián, Spain. [12]Centro de Física de Materiales (CSIC-UPV/EHU), Donostia/San Sebastián, Spain. [13]IKERBASQUE, Basque Foundation for Science, Bilbao, Spain. ✉e-mail: javiermartin@uniovi.es; pabloalonso@uniovi.es

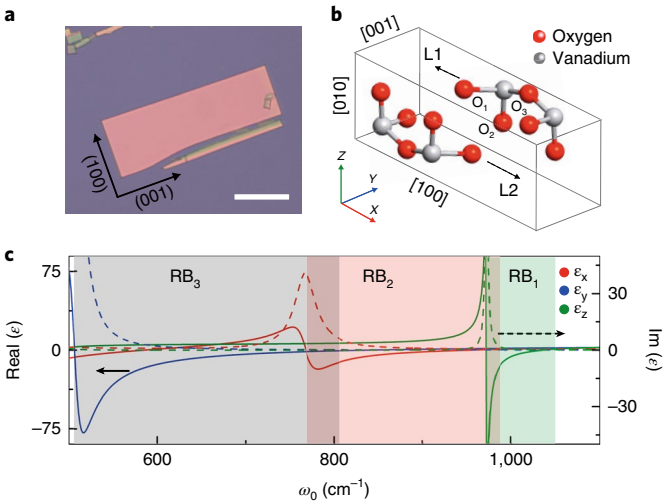

Fig. 1 | Physical properties of α-V_2O_5. a, Optical image of an α-V_2O_5 flake. α-V_2O_5 crystals show a rectangular shape owing to their anisotropic crystal structure. Labelled arrows indicate the [100] and [001] crystal directions. Scale bar, 10 μm. **b**, Schematic of the crystalline unit cell of α-V_2O_5; the lattice constants along the principal *x*, *y* and *z* axes are $a = 1.15$, $b = 0.36$ and $c = 0.44$ nm, respectively. Grey spheres represent the vanadium atoms and red spheres represent the oxygen atoms. The three oxygen positions of asymmetric V–O bonds along different crystalline axes are denoted $O_{1\text{-}3}$. L1 and L2 indicate the two vdW layers weakly bound along the [010] crystal direction. **c**, Real (continuous lines) and imaginary part (dashed lines) of the permittivity (see Methods) along the principal *x* ([100]), *y* ([001]) and *z* ([010]) axes (red, blue and green lines, respectively). The Reststrahlen bands RB_1, RB_2 and RB_3 are indicated in green, red and grey, respectively.

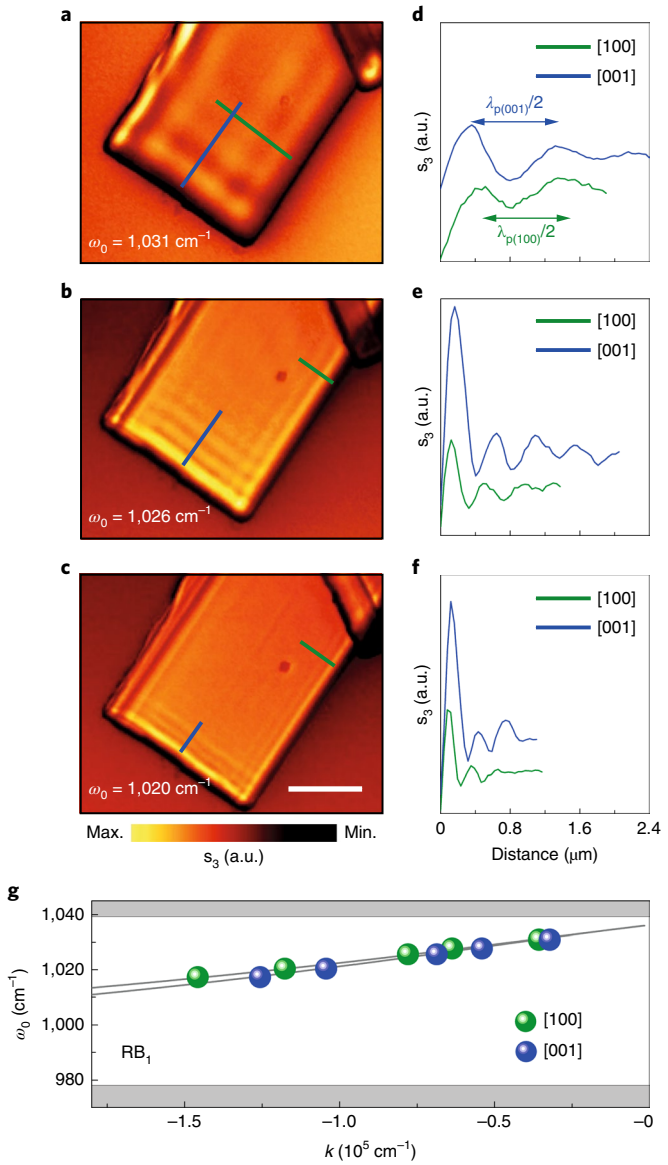

Fig. 2 | Real-space imaging of a α-V_2O_5 flake. a–**c**, Near-field amplitude images s_3 of an α-V_2O_5 flake with thickness $d = 105$ nm at incident frequencies $\omega_0 = 1{,}031$ (**a**), 1,026 (**b**) and 1,020 cm^{-1} (**c**). Scale bar in **c**, 2 μm. **d**–**f**, Profiles along the [100] (green lines) and [001] (blue lines) directions, extracted from the near-field amplitude images in **a**–**c**, respectively. $\lambda_{p[100]}$ and $\lambda_{p[001]}$ are the polariton wavelengths along the [100] and [001] directions, respectively. **g**, Dispersion of PhPs along the [100] (green symbols) and [001] (blue symbols) directions in the RB_1. Grey lines are guides for the eye. Grey shaded areas indicate the spectral regions outside the RB. a.u., arbitrary units.

optical microscopy (s-SNOM), which yields nanoscale resolved near-field images together with sample topography (Methods). In Fig. 2a–c we show near-field amplitude images of an α-V_2O_5 flake with thickness $d = 105$ nm, taken at frequencies belonging to RB_1 of α-V_2O_5: $\omega_0 = 1{,}031$, $\omega_0 = 1{,}026$ and $\omega_0 = 1{,}020$ cm^{-1}, respectively. In the images we observe bright fringes parallel to all flake edges, but with different periodicities depending on the crystal direction, indicating PhPs with in-plane (along the flake) anisotropic propagation[2,5]. This can be better examined by analysing the profiles shown on the right of the s-SNOM images, for example, in Fig. 2e, where the polariton wavelength λ_p is about 915 nm along the [100] crystal direction and about 800 nm along the [001] direction (note that in polariton interferometry[18,19] the polaritons excited by the tip propagate away and are back-reflected at the flake edges, giving rise to interference fringes with a spacing $\lambda_p/2$), clearly corroborating an in-plane anisotropic propagation of PhPs. Apart from this extraordinary behaviour, the PhPs wavelengths along the [100] and [001] directions also reveal a deep subwavelength-scale polariton confinement $\lambda_p \ll \lambda_0 = 9.75$ μm (where λ_0 is the infrared illuminating wavelength), which is a key characteristic for their potential use in nanophotonics.

The in-plane anisotropic propagation of PhPs in α-V_2O_5 can be more clearly observed by plotting the dispersions $\omega(k_i)$ ($i = x$, y, corresponding to the [100] and [001] crystal directions) extracted from s-SNOM images taken at single incident frequencies (Fig. 2g). Although they follow similar slopes, there is a clear separation between them verifying that PhPs in RB_1 propagate with in-plane anisotropy. The PhPs' phase velocity, $v_{p,i} = \omega_0/k_i$, can be also extracted by plotting the complex-valued wavevector (Supplementary Information), being negative for both directions. Also, the slopes of the dispersion curves (Supplementary Information) give us information on their group velocities ($v_{g,i} = \partial k_i/\partial\omega)^{-1}$), which turn out to be very small (about 0.0009 *c*, with *c* the speed of light in vacuum) in both directions (at $\omega_0 = 1{,}026$ cm^{-1}, see Supplementary Information), showing potential for applications involving light–matter interactions[20].

To better describe the properties of PhPs in α-V_2O_5, we performed nanoscale Fourier-transform infrared spectroscopy[2,21] (nanoFTIR) measurements (Methods) along the [100] and [001] in-plane crystal directions (Fig. 3b, left and right panels, respectively). We observed three spectral bands ($RB_{1\text{-}3}$) exhibiting a series of signal maxima within band limits corresponding to longitudinal

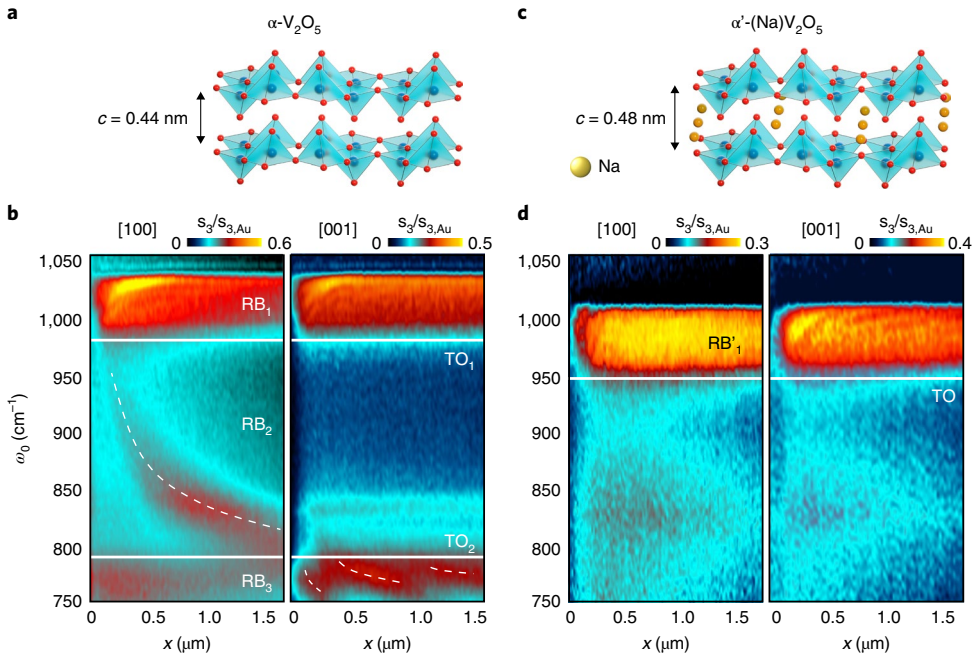

Fig. 3 | Real-space nano-spectroscopy of α-V_2O_5 and intercalated α'-(Na)V_2O_5 flakes. a, Illustration of the α-V_2O_5 lattice structure (orthorhombic) where the red spheres represent oxygen atoms, the blue atoms represent vanadium atoms, and the blue pyramids show the polyhedral structure defined by the oxygen atoms. The crystal structure consists of bilayers of distorted VO_5 pyramids stacked along the [010] direction via vdW interactions (interlayer distance $c = 0.44$ nm). **b**, nanoFTIR spectral line scans along the [100] and [001] directions of a α-V_2O_5 flake showing $s_3/s_{3,Au}$ (near-field amplitude s_3 normalized on Au, $s_{3,Au}$) as a function of distance between the tip and the flake edge. Solid horizontal lines mark the approximate transversal optic (TO) phonon modes in α-V_2O_5 (TO_1, 975 cm^{-1}; TO_2, 770 cm^{-1}), separating RB_{1-3}. Dashed lines are guides for the eye of signal maxima. The flake thickness is $d = 245$ nm. **c**, Illustration of the α'-(Na)V_2O_5 lattice structure (orthorhombic) where the red spheres represent oxygen atoms, the blue atoms represent vanadium atoms, the yellow atoms represent sodium atoms and the blue pyramids show the polyhedral structure defined by the oxygen atoms. The crystal structure consists of bilayers of distorted VO_5 pyramids with sodium atoms intercalated and stacked along the [010] direction via vdW interactions (interlayer distance $c = 0.48$ nm). **d**, nanoFTIR spectral line scans along the [100] and [001] directions of a α'-(Na)V_2O_5 flake showing $s_3/s_{3,Au}$ (near-field amplitude s_3 normalized on Au, $s_{3,Au}$) as a function of distance between the tip and the flake edge. The solid horizontal line approximately mark the transversal optic phonon mode in α'-(Na)V_2O_5 (TO, 950 cm^{-1}), defining RB'_1. The flake thickness is $d = 150$ nm. The scales in the colour bars of **b** and **d** are linear.

and transverse optic phonon frequencies of α-V_2O_5 (RB_{1-3} in Fig. 1c, Supplementary Information) unveiling the existence of PhPs. In RB_1 we find that (1) the signal maxima show a different spacing (corresponding to λ_p) along both [100] and [001] directions, and that (2) λ_p increases with the frequency. These observations further reveal the in-plane anisotropic (elliptic) propagation and negative phase velocity of PhPs in the RB_1 of α-V_2O_5. In contrast, in RB_2 we find that (1) the signal maxima (dashed line in the figure) are only present along the [100] direction (there are no visible fringes along the [001] direction) and that (2) λ_p decreases with the frequency. These observations indicate the excitation of PhPs with in-plane hyperbolic propagation and positive v_p. Finally, in RB_3 we find fringes, indicated by signal maxima (dashed lines in the figure), only along the [001] crystal direction (there are no visible fringes along the [100] direction), which points out to a similar in-plane hyperbolic behaviour to that in RB_2 but along the orthogonal direction. Overall, these nanoFTIR results confirm that α-V_2O_5 supports PhPs with in-plane anisotropic propagation (elliptic and hyperbolic along both orthogonal directions), thus adding another member to the library of vdW materials supporting PhPs[2,4,5].

As a metal oxide, α-V_2O_5, offers the possibility of being efficiently intercalated with alkali ions[22], which entails attractive prospects for energy technologies[23]. Intercalation has been recently demonstrated to be a promising low-temperature synthesis strategy to tune the physical and chemical properties of vdW materials such as MoS_2 (ref. [24]), Bi_2Se_3 (ref. [25]) or black phosphorus[26]. However, the effect of intercalation on the polaritonic response of a layered crystal has been barely studied, being a switching capability (originated by inducing a minimal polariton propagation in the intercalated area) together with a RB shift of a few wavenumbers the only polaritonic effects reported so far[4]. In the following, we study the effects of intercalation (using Na atoms by single crystal growth (Methods), different from previous works based on aqueous solutions[4]) on the polaritonic response of α-V_2O_5. Figure 3d shows nanoFTIR line scans along the [100] and [001] in-plane directions (left and right panels, respectively) of an intercalated α'-(Na)V_2O_5 flake. We observe a spectral band, RB'_1, that appears clearly red-shifted with respect to RB_1 in α-V_2O_5, and that shows periodic fringes of signal maxima indicating the existence of PhPs. These periodic signal maxima show a different spacing along the [100] and [001] directions, which increases with the frequency, revealing PhPs with in-plane anisotropic propagation (elliptic) and negative phase velocity in α'-(Na)V_2O_5. They are thus similar to PhPs in RB_1 of pristine α-V_2O_5 but shifted to smaller frequencies. To better analyse this effect we plot in Fig. 4a the dispersions extracted from several monochromatic s-SNOM images for both pristine and intercalated flakes (Methods). We can clearly observe that the dispersion of PhPs in RB'_1 (with its limits marked by dark green lines) of intercalated α'-(Na)V_2O_5 is strongly red-shifted (about 30 cm^{-1} from centre to centre of both RBs), in comparison to the dispersion of PhPs in RB_1 of α-V_2O_5 (with its limits marked by bright green lines). This finding unambiguously demonstrates that a broad spectral shift of a RB

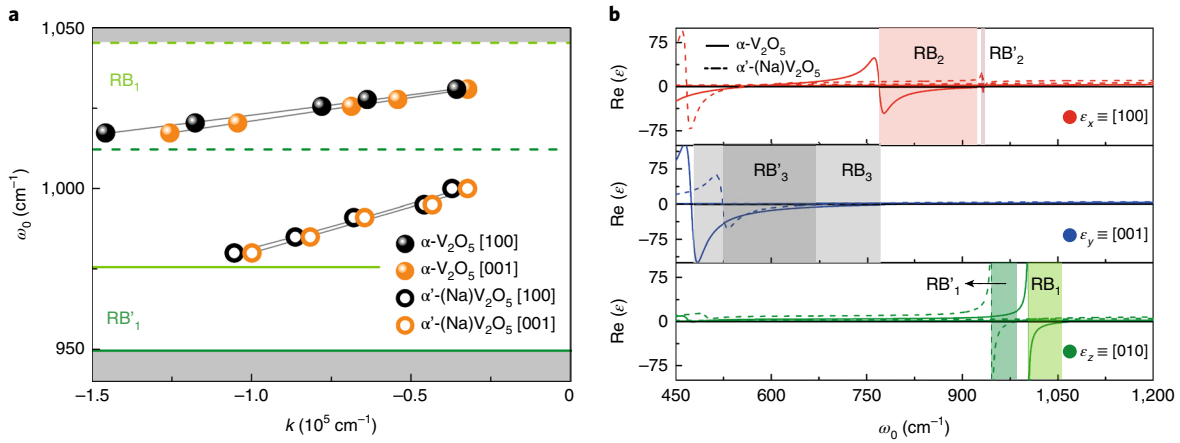

Fig. 4 | PhPs dispersion and ab initio permittivity in α-V_2O_5 and intercalated α'-(Na)V_2O_5 crystals. a, Dispersion of PhPs along the [100] and [001] directions in an α-V_2O_5 (full symbols) flake with thickness $d = 105$ nm and an α'-(Na)V_2O_5 (empty symbols) flake with thickness $d = 190$ nm. Dashed and continuous horizontal lines mark the approximate transverse and longitudinal optic phonon modes in α-V_2O_5 (transverse optic, 980 cm^{-1}; longitudinal optic, 1,040 cm^{-1}) and α'-(Na)V_2O_5 (transverse optic, 945 cm^{-1} and longitudinal optic, 1,015 cm^{-1}), respectively. Grey lines are guides for the eye. Grey shaded areas indicate the spectral regions outside the RBs. **b**, Real part of the permittivities for α-V_2O_5 (continuous lines) and α'-(Na)V_2O_5 (dashed lines) extracted from ab initio calculations along the principal *x*, *y* and *z* axes (red, blue and green lines, respectively). The Reststrahlen bands RB_{1-3}, and RB'_{1-3} for α-V_2O_5 and α'-(Na)V_2O_5, are indicated in bright and dark shading, respectively. Green shaded regions represent RB_1 and RB'_1; red shaded regions represent RB_2 and RB'_2 and grey shaded regions represent RB_3 and RB'_3.

can be originated by the intercalation of Na atoms into α-V_2O_5, thus demonstrating a key property for PhPs: spectral tunability via intercalation of the host material.

We note that the nanoFTIR image in Fig. 3d does not show any indication of other RBs that could be associated to RB_2 or RB_3 of α-V_2O_5. To better understand the polaritonic effects induced by the intercalation of Na atoms into α-V_2O_5 and the spectral shift obtained, we calculate from first principles (Supplementary Information) the phonon dispersions of α-V_2O_5 and α'-(Na)V_2O_5 crystals. The crystalline structures used in the calculations are illustrated in Fig. 3, where the typical orthorhombic structure of α-V_2O_5 (Fig. 3a) is modified by the intercalation of Na atoms preferentially located in between the vdW layers (Fig. 3c). The extracted phonon modes (Supplementary Information) are then used in a Lorentz oscillators model to retrieve the theoretical permittivities for both crystalline structures, which are plotted in Fig. 4b. In the plotted range, α-V_2O_5 shows three RBs (RB_{1-3} in the figure) in qualitative agreement with the experimental permittivity shown in Fig. 1c, thus validating our ab initio calculations. For α'-(Na)V_2O_5 we also obtain three RBs (RB'_{1-3}), yet narrower and centred at shifted frequencies with respect to RB_{1-3}, respectively. In particular, RB'_1 appears red-shifted for about 50 cm^{-1} (from centre to centre) in good agreement with our results shown in the nanoFTIR images in Fig. 3. On the other hand, mainly due to a modification of the oxygen effective charges along the [100] direction, RB'_2 appears blue-shifted and far narrower, to the point of being almost imperceptible, which explains its absence in our experiments. Finally, RB'_3 appears also narrower due to the longitudinal optic phonon frequency being strongly red-shifted, which also explains its absence in our measurements in Fig. 3d as it lays out of our nanoFTIR spectral range.

Apart from the spectral shifts induced in the RBs (and thus in the PhPs' dispersions), the intercalation of Na atoms into the α-V_2O_5 crystal lattice might have an influence on the PhPs' anisotropic propagation and, more importantly, on their lifetimes. To compare the propagation of PhPs in α-V_2O_5 and α'-(Na)V_2O_5, we fabricated a metal antenna (gold disk) on top of both crystals and imaged their polaritonic activity by s-SNOM at frequencies in RB_1 and RB'_1, respectively (Fig. 5a,b). Due to its circular geometry, the gold disk can act as an efficient launcher of PhPs along all directions in the

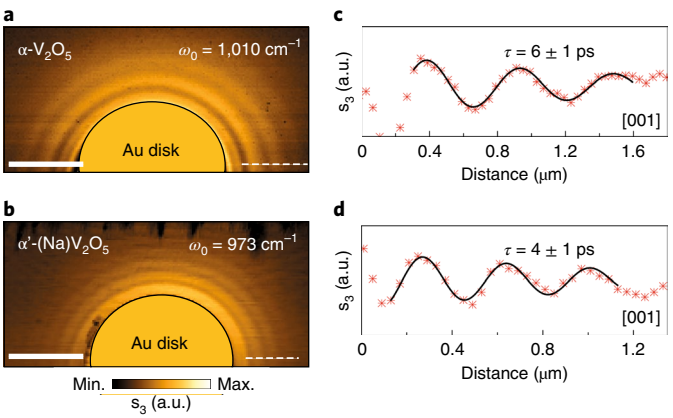

Fig. 5 | Anisotropy and lifetimes of PhPs in α-V_2O_5 and intercalated α'-(Na)V_2O_5 flakes. a,**b**, Near-field amplitude images s_3 of α-V_2O_5 and α'-(Na)V_2O_5 flakes with thicknesses $d = 130$ and $d = 107$ nm at illuminating frequencies $\omega_0 = 1{,}010$ cm^{-1} (RB_1; **a**) and $\omega_0 = 973$ cm^{-1} (RB'_1; **b**). A gold disk (half of it shown in the image for convenience) is used as an antenna for efficient launching of PhPs along all in-plane directions. Scale bars, 2 μm. **c**,**d**, s-SNOM line traces (showing the amplitude s-SNOM signal s_3, Methods) along the [001] direction of α-V_2O_5 and α'-(Na)V_2O_5 flakes indicated by white dashed lines in **a** (**c**) and **b** (**d**). Damped sine-wave functions (black solid lines) were fitted to the data (Supplementary Information). Lifetimes of $\tau = 6 \pm 1$ and $\tau = 4 \pm 1$ ps are obtained, respectively.

plane, thus enabling a direct investigation of the PhPs propagation. In both crystals we observe fringes along all directions in the plane, corresponding to the excitation of PhPs[27], which show a slightly longer λ_p along the [001] direction, revealing similar in-plane elliptic propagation in both crystals. From this, we can draw the conclusion that intercalation has a negligible effect on the in-plane anisotropic propagation of PhPs in α-V_2O_5.

Finally, we study and compare the PhPs' lifetimes in both pristine α-V_2O_5 and intercalated α'-(Na)V_2O_5 crystals, which is crucial for validating intercalation as an effective material synthesis strat-

egy for nanophotonics. To do this, we extracted s-SNOM line profiles (red crosses in Fig. 5c,d, taken at $\omega_0 = 1{,}010$ and $\omega_0 = 973\,cm^{-1}$, respectively) along the [001] direction of the α-V_2O_5, and α'-(Na)V_2O_5 flakes with similar thicknesses of 130 and 107 nm, shown in Fig. 5a,b, respectively. By fitting them with an exponentially decaying sine-wave function corrected by the geometrical spreading factor[2,28] $\sqrt{x}$ (Supplementary Information) we extract decay lengths $L_{p[001]}$ of 1.40 μm for α-V_2O_5 PhPs (yielding a propagation figure of merit[3] $Q = \mathrm{Re}(k)/\mathrm{Im}(k)$ of 3.5) and 1.15 μm for α'-(Na)V_2O_5 PhPs (yielding $Q = 2.5$). With these values, we obtain the lifetimes according to $\tau_{[001]} = L_{[001]}/v_g$, where the group velocities v_g are taken from the PhPs' dispersions (Supplementary Fig. S4). We obtain $\tau_{[001]} = 6 \pm 1$ ps for PhPs in α-V_2O_5, and $\tau_{[001]} = 4 \pm 1$ ps for PhPs in intercalated α'-(Na)V_2O_5. These notable lifetime values (obtained despite a short L_p due to the ultra-slow PhP's group velocity of 0.0007c) reveal the low-loss nature of PhPs in α-V_2O_5, which can be related to the fact that α-V_2O_5 is close to being isotopically pure, since natural abundance oxygen and vanadium have both isotopic purities of 99.7%, and; more importantly, that the intercalation process followed in this work not only allows for a large spectral shift of PhPs, but also for preserving their low-loss nature (despite a reduction upon intercalation, the PhPs' lifetimes are still in the picosecond range).

In conclusion, this work demonstrates intercalation of atoms (Na) in a vdW crystal (α-V_2O_5) as an efficient technological approach to achieve a broad spectral shift of PhPs with ultra-long lifetimes. Considering that a large variety of ions and ion contents can be intercalated in layered materials[29], we envision on-demand spectral response of PhPs in vdW materials, eventually allowing for covering the whole mid-infrared range, critical for the emerging field of PhP photonics. We also note that α-V_2O_5, as a semiconductor, can be electrically doped to support plasmon polaritons, which, via coupling to longitudinal optic phonons[30], could eventually allow for a dynamic tuning of PhPs spectrally shifted by intercalation.

Online content

Any methods, additional references, Nature Research reporting summaries, source data, extended data, supplementary information, acknowledgements, peer review information; details of author contributions and competing interests; and statements of data and code availability are available at https://doi.org/10.1038/s41563-020-0665-0.

Received: 14 November 2019; Accepted: 6 March 2020;
Published online: 13 April 2020

References

1. Dai, S. et al. Tunable phonon polaritons in atomically thin van der Waals crystals of boron nitride. *Science* **343**, 1125–1129 (2014).
2. Ma, W. et al. In-plane anisotropic and ultra-low-loss polaritons in a natural van der Waals crystal. *Nature* **562**, 557–562 (2018).
3. Giles, A. J. et al. Ultralow-loss polaritons in isotopically pure boron nitride. *Nat. Mater.* **17**, 134–139 (2017).
4. Zheng, Z. et al. Highly confined and tunable hyperbolic phonon polaritons in van der waals semiconducting transition metal oxides. *Adv. Mat.* **30**, 1705318 (2018).
5. Zheng, Z. et al. A mid-infrared biaxial hyperbolic van der Waals crystal. *Sci. Adv.* **5**, eaav8690 (2019).
6. Low, T. et al. Polaritons in layered two-dimensional materials. *Nat. Mater.* **16**, 182 (2016).
7. Basov, D. N., Fogler, M. M. & García de Abajo, F. J. Polaritons in van der Waals materials. *Science* **354**, aag1992 (2016).
8. Li, P. et al. Reversible optical switching of highly confined phonon-polaritons with an ultrathin phase-change material. *Nat. Mater.* **15**, 870–875 (2016).
9. Sukimura, H. et al. Highly confined and switchable mid-infrared surface phonon polariton resonances of planar circular cavities with a phase change material. *Nano Lett.* **19**, 2549–2554 (2019).
10. Caldwell, J. D. et al. Photonics with hexagonal boron nitride. *Nat. Rev. Mater.* **4**, 552–567 (2019).
11. Dunkelberger, A. D. et al. Active tuning of surface phonon polariton resonances via carrier photoinjection. *Nat. Photonics* **12**, 50–56 (2018).
12. Ratchford, D. C. et al. Controlling the infrared dielectric function through atomic-scale heterostructures. *ACS Nano* **13**, 6730–6741 (2019).
13. Bhandari, C. & Lambrecht, W. R. L. Phonons and related spectra in bulk and monolayer V_2O_5. *Phys. Rev. B.* **89**, 045109 (2014).
14. Sucharitakul, S. et al. V2O5: A 2D van der waals oxide with strong in-plane electrical and optical anisotropy. *ACS Appl. Mater. Interfaces* **9**, 23949–23956 (2017).
15. Clauws, P. & Vennik, J. Lattice vibrations of V_2O_5. Determination of TO and LO frequencies from infrared reflection and transmission. *Phys. Status Solidi* **76**, 707–713 (1976).
16. Gomez-Diaz, J. S. & Alù, A. Flatland optics with hyperbolic metasurfaces. *ACS Photonics* **3**, 2211–2224 (2016).
17. Gomez-Diaz, J. S., Tymchenko, M. & Alù, A. Hyperbolic plasmons and topological transitions over uniaxial metasurfaces. *Phys. Rev. Lett.* **114**, 233901 (2015).
18. Chen, J. et al. Optical nano-imaging of gate-tunable graphene plasmons. *Nature* **487**, 77–81 (2012).
19. Fei, Z. et al. Gate-tuning of graphene plasmons revealed by infrared nano-imaging. *Nature* **487**, 82–85 (2012).
20. Autore, M. et al. Boron nitride nanoresonators for phonon-enhanced molecular vibrational spectroscopy at the strong coupling limit. *Light.: Sci. Appl.* **14**, 17172 (2018).
21. Huth, F., Schnell, M., Wittborn, J., Ocelic, N. & Hillenbrand, R. Infrared-spectroscopic nanoimaging with a thermal source. *Nat. Mater.* **10**, 352–356 (2011).
22. Braithwaite, J. S., Catlow, C. R. A., Gale, J. D. & Harding, J. H. Lithium intercalation into vanadium pentoxide: a theoretical study. *Chem. Mater.* **11**, 1990–1998 (1999).
23. Liu, J., Xia, H., Xue, D. & Lu, L. Double-shelled nanocapsules of V_2O_5-based composites as high-performance anode and cathode materials for Li ion batteries. *J. Am. Chem. Soc.* **131**, 12086–12087 (2009).
24. Xiong, F. et al. Li intercalation in MoS_2: in situ observation of its dynamics and tuning optical and electrical properties. *Nano Lett.* **15**, 6777–6784 (2015).
25. Cha, JudyJ. et al. Two-dimensional chalcogenide nanoplates as tunable metamaterials via chemical intercalation. *Nano Lett.* **13**, 5913–5918 (2013).
26. Zhang, R., Waters, J., Geim, A. K. & Grigorieva, I. V. Intercalant-independent transition temperature in superconducting black phosphorus. *Nat. Commun.* **8**, 15036 (2017).
27. Pons-Valencia, P. et al. Launching of hyperbolic phonon-polaritons in h-BN slabs by resonant metal plasmonic antennas. *Nat. Commun.* **10**, 3242 (2019).
28. Woessner, A. et al. Highly confined low-loss plasmons in graphene–boron nitride heterostructures. *Nat. Mater.* **14**, 421–425 (2014).
29. Kwabena Bediako, D. Heterointerface effects in the electrointercalation of van der Waals heterostuctures. *Nature* **558**, 425–429 (2018).
30. Talwar, N. T. Direct evidence of LO phonon-plasmons coupled modes in n-GaN. *Appl. Phys. Lett.* **97**, 051902 (2010).

Methods

s-SNOM. The infrared nanoimaging and nanoFTIR measurements were performed according to previous work (ref. [2]) and reproduced here for completeness. We used a s-SNOM (from Neaspec) for infrared nanoimaging. This system employed a Pt–Ir coated atomic force microscope (AFM) tip illuminated with infrared light as a launcher and recorder of polaritons, yielding simultaneously near-field images and topography. The metallized AFM tip was illuminated with light (p polarized) of frequency, ω, from a quantum cascade laser. The tip oscillated at a frequency $\Omega \approx 270$ kHz with an amplitude of about 100 nm. The tip-launched polaritons reflected at the V_2O_5 flake edges and produced polariton standing wave interferences, which were imaged by recording the light scattered by the tip. This was carried out with a pseudo-heterodyne interferometer that demodulated the detector signal at high harmonics, $n\Omega$ (typically third harmonics, named s_3), and provided background-free detection. The metal coated AFM tip provided wavelength-independent resolution.

nanoFTIR. For the nanoFTIR images, we employed the nanoFTIR module for the s-SNOM system. We used an Au coated AFM tip illuminated by a super-continuum laser and the scattered light was recorded with an asymmetric Fourier-transform spectrometer. Spectral line scans were obtained by recording point spectra as a function of the tip position.

α-V_2O_5 and α'-(Na)V_2O_5 sample growth and preparation. Orthorhombic layered α-V_2O_5 with a vdW structure was synthesized via a purification method and subsequent single crystal growth, as described in refs. [14,31]. Sodium-intercalated α'-(Na)V_2O_5 single crystals were grown in a similar way as described in ref. [32]. Briefly, a mixture of $NaVO_3$ (1.843 g) and VO_2 (0.1564 g) powder was put into a Pt crucible with a lid and sealed under vacuum in a quartz tube. The mixture was heated to 800 °C at a rate of 100 °C h^{-1} and kept at 800 °C for 0.5 h. It was then cooled to 740 °C at a rate of 1 °C h^{-1}, kept at 740 °C for 3 d, slowly cooled to 600 °C at a rate of 1.5 °C h^{-1} and finally cooled to room temperature at a rate of 300 °C h^{-1} to yield α'-(Na)V_2O_5 crystals. Temperature dependent magnetic susceptibility measurement of the as-grown α'-(Na)V_2O_5 crystal verified a spin-Peierls transition at ~35 K, in agreement with the literature[32] indicating adequately intercalated α'-(Na)V_2O_5. Bulk α-V_2O_5 and α'-(Na)V_2O_5 crystals were thinned down by mechanical exfoliation using Nitto blue tape leading to thin slabs with thicknesses in the range of 100 nm to a few micrometres, which were transferred on top of a 300-nm-thick SiO_2 layer deposited on a Si substrate. For maximum yield of thin crystals, the substrates were heated to 90 °C for 10 min during the transfer.

Dielectric function of α-V_2O_5. The principal values of the diagonal permittivity tensor, ε_x, ε_y and ε_z, are approximated with a three-parameter Drude–Lorentz permittivity:

$$\varepsilon_{a(\omega)} = \varepsilon_{a,\infty} \frac{\left(\omega_{\mathrm{LO}}^{a}\right)^2 - \omega^2 + i\gamma^a \omega_{\mathrm{LO}}^{a} \omega}{\left(\omega_{\mathrm{TO}}^{a}\right)^2 - \omega^2 + i\gamma^a \omega_{\mathrm{TO}}^{a} \omega},$$

where $a = x,y,z$, ω_{TO} and ω_{LO} refer to the transversal and longitudinal phonon frequencies, respectively, γ denotes the damping constant and $\varepsilon_{a,\infty}$ is the high frequency permittivity. The values of the constants are: $\omega_{\mathrm{TO}}^{x} = 765\ \mathrm{cm}^{-1}$, $\omega_{\mathrm{LO}}^{x} = 952\ \mathrm{cm}^{-1}$, $\gamma^x = 40\ \mathrm{cm}^{-1}$, $\varepsilon_{x\infty} = 6.6$; $\omega_{\mathrm{TO}}^{y} = 506\ \mathrm{cm}^{-1}$, $\omega_{\mathrm{LO}}^{y} = 842\ \mathrm{cm}^{-1}$, $\gamma^y = 19\ \mathrm{cm}^{-1}$, $\varepsilon_{y\infty} = 6.1$ and $\omega_{\mathrm{TO}}^{z} = 976\ \mathrm{cm}^{-1}$, $\omega_{\mathrm{LO}}^{z} = 1{,}037\ \mathrm{cm}^{-1}$, $\gamma^z = 2.0/1.5\ \mathrm{cm}^{-1}$ and $\varepsilon_{z\infty} = 3.9$.

The values of ω_{LO}^{a} and ω_{TO}^{a} were adjusted by fitting FTIR and s-SNOM measurements with transfer-matrix calculations, while $\varepsilon_{a,\infty}$ were obtained from ab initio calculations (Supplementary Information). The values of γ^a were taken from ref. [15]. $\gamma^z = 1.5\ \mathrm{cm}^{-1}$ is also considered (Supplementary Information) to better fit the experimental lifetime values and in analogy to ref. [33].

Structural characterization. α-V_2O_5 and α'-(Na)V_2O_5 local structures were analysed by high-resolution transmission electron microscopy using a Tecnai F20 ST (FEI) operating at 200 kV. X-ray diffraction was performed using a Bruker Discover D8 with VÅNTEC-500 solid state detector, using a Co K-alpha X-ray source with a wavelength of 1.788 nm.

Data availability

The data represented in Figs. 1–5 are provided with the paper as source data. All other data that support results in this Letter are available from the corresponding author on reasonable request.

Code availability

The custom code employed in this work to perform all calculations is available from the corresponding authors on reasonable request.

References

31. Haemers, J. Purification and single crystal growth of V_2O_5. *Bull. des. Soci. Chim. Belg.* **79**, 473–477 (1970).
32. Isobe, M., Kagami, C. & Ueda, Y. Crystal growth of new spin-Peierls compound NaV_2O_5. *J. Cryst. Growth* **181**, 314–317 (1997).
33. Álvarez-Pérez, G. et al. Infrared permittivity of the biaxial van der Waals semiconductor α-MoO3 from near- and far-field correlative studies. Preprint at https://arxiv.org/abs/1912.06267 (2019).

Acknowledgements

J.T.-G. and G.Á.-P. acknowledge support through the Severo Ochoa Program from the Government of the Principality of Asturias (nos. PA-18-PF-BP17-126 and PA-20-PF-BP19-053, respectively). J.M.-S. acknowledges finantial support from the Clarín Programme from the Government of the Principality of Asturias and a Marie Curie-COFUND grant (PA-18-ACB17-29) and the Ramón y Cajal Program from the Government of Spain (RYC2018-026196-I). K.C., X.P.A.G., H.V. and M.H.B. acknowledge the Air Force Office of Scientific Research (AFOSR) grant no. FA 9550-18-1-0030 for funding support. I.E. acknowledges financial support from the Spanish Ministry of Economy and Competitiveness (grant no. FIS2016-76617-P). A.Y.N. acknowledges the Spanish Ministry of Science, Innovation and Universities (national project no. MAT2017-88358-C3-3-R) and the Basque Government (grant no. IT1164-19). Q.B. acknowledges the support from Australian Research Council (grant nos. FT150100450, IH150100006 and CE170100039). R.H. acknowledges support from the Spanish Ministry of Economy, Industry, and Competitiveness (national project RTI2018-094830-B-100 and the Project MDM-2016-0618 of the María de Maeztu Units of Excellence Program) and the Basque Goverment (grant no. IT1164-19). P.A.-G. acknowledges support from the European Research Council under starting grant no. 715496, 2DNANOPTICA.

Author contributions

P.A.-G. and J.T.-G. conceived the study. P.A.-G. and J.M.-S. supervised the project. J.T.-G. and J.D. carried out the near-field imaging experiments with the help of M.A., S.L. and W.M. G.A.-P., A.B., R.H., Q.B. and A.Y.N. participated in data analysis. P.A.-G. wrote the manuscript with input from J.T.-G., G.A.-P., J.M.-S., A.N., J.D., Q.B., I.E., X.P.A.G., K.C. and R.H. I.E. carried out ab initio calculations. G.A.-P. and A.Y.N. conducted the analytical calculations. K.K., T.K., K.C. and X.P.A.G. contributed to material synthesis and sample preparation. H.V. and M.H.B. performed the transmission electron microscopy characterization. K.C. performed X-ray diffraction indexing and characterization. I.P. contributed to sample fabrication.

Competing interests

R.H. is cofounder of Neaspec GmbH, a company producing s-SNOM systems, such as the one used in this study. The remaining authors declare no competing interests.

Additional information

Supplementary information is available for this paper at https://doi.org/10.1038/s41563-020-0665-0.

Correspondence and requests for materials should be addressed to J.M.-S. or P.A.-G.

Reprints and permissions information is available at www.nature.com/reprints.